



Sedimentation of an ellipsoidal particle in narrow tubes

Haibo Huang, Xin Yang, and Xi-yun Lu

Citation: *Physics of Fluids* (1994-present) **26**, 053302 (2014); doi: 10.1063/1.4874606

View online: <http://dx.doi.org/10.1063/1.4874606>

View Table of Contents: <http://scitation.aip.org/content/aip/journal/pof2/26/5?ver=pdfcov>

Published by the [AIP Publishing](#)

Articles you may be interested in

[Suspension flow and sedimentation in self-affine fractures](#)

Phys. Fluids **24**, 053303 (2012); 10.1063/1.4717529

[First-order virial expansion of short-time diffusion and sedimentation coefficients of permeable particles suspensions](#)

Phys. Fluids **23**, 083303 (2011); 10.1063/1.3626196

[Direct Numerical Simulation of Polygonal Particles Sedimentation with Collisions](#)

AIP Conf. Proc. **1027**, 944 (2008); 10.1063/1.2964903

[Asymptotic analysis of chaotic particle sedimentation and trapping in the vicinity of a vertical upward streamline](#)

Phys. Fluids **19**, 073302 (2007); 10.1063/1.2751387

[Dynamics of particle sedimentation in a vertical channel: Period-doubling bifurcation and chaotic state](#)

Phys. Fluids **15**, 1612 (2003); 10.1063/1.1571825



Re-register for Table of Content Alerts

Create a profile.



Sign up today!



Sedimentation of an ellipsoidal particle in narrow tubes

Haibo Huang,^{a)} Xin Yang, and Xi-yun Lu

Department of Modern Mechanics, University of Science and Technology of China, Anhui 230026, China

(Received 15 February 2014; accepted 17 April 2014; published online 7 May 2014)

Sedimentation behaviours of an ellipsoidal particle in narrow and infinitely long tubes are studied by a multi-relaxation-time lattice Boltzmann method (LBM). In the present study, both circular and square tubes with $12/13 \leq D/A \leq 2.5$ are considered with the Galileo number (Ga) up to 150, where D and A are the width of the tube and the length of major axis of the ellipsoid, respectively. Besides three modes of motion mentioned in the literature, two novel modes are found for the narrow tubes in the higher Ga regime: the spiral mode and the vertically inclined mode. Near a transitional regime, in terms of average settling velocity, it is found that a lighter ellipsoid may settle faster than a heavier one. The relevant mechanism is revealed. The behaviour of sedimentation inside the square tubes is similar to that in the circular tubes. One significant difference is that the translation and rotation of ellipsoid are finally constrained to a diagonal plane in the square tubes. The other difference is that the anomalous rolling mode occurs in the square tubes. In this mode, the ellipsoid rotates as if it is contacting and rolling up one corner of the square tube when it settles down. Two critical factors that induce this mode are identified: the geometry of the tube and the inertia of the ellipsoid. © 2014 AIP Publishing LLC. [<http://dx.doi.org/10.1063/1.4874606>]

I. INTRODUCTION

There are a variety of studies on the motion of non-spherical particles in a viscous fluid.¹⁻⁴ Jeffery studied the rotational modes of an ellipsoid in Couette flow under Stokes flow conditions.¹ Cox investigated the steady motion of a particle of arbitrary shape at small Reynolds numbers (Re) analytically.⁵ Russel *et al.* dealt with the motion of an inertia-less rod-like object falling near a flat wall in Stokes flow.⁶ They concluded that the rod undergoes a periodic motion between two parallel plates. Broday *et al.* studied the motion of non-neutrally buoyant spheroidal particles in vertical unbounded shear flows under creeping-flow conditions.³ They found that inertia effect plays an important role on a particle's behavior. A detailed review of the study of the motion of non-spherical particles before 1998 can be found in Ref. 3.

Over the last 30 years, different numerical methods have been developed to study the motion of particles in a viscous fluid. Brady and Bossis adapted the Stokesian dynamics method for simulating the motion of many particles in Stokes flow.⁷ However, this method is only applicable to spherical particles and it neglects the inertial term. For finite-Reynolds-number flows the Navier-Stokes equations have to be solved. Sugihara-Seki studied numerically the motions of an inertia-less elliptical particle in a tube flow using a Finite Element (FE) method.⁸ Swaminathan *et al.* studied the sedimentation of an ellipsoid inside an infinitely long tube at low and intermediate Reynolds numbers.⁹ They used an arbitrary Lagrangian-Eulerian (ALE)-based FE method coupled with a body-fitted moving finite-element mesh. Fictitious domain schemes are also a useful numerical tool to simulate solid-liquid flow.¹⁰

The application of lattice Boltzmann methods (LBMs) to study the motion of non-spherical particles has been well established.¹¹⁻¹³ In the LBM, the Poisson equation is not required to be

^{a)} Author to whom correspondence should be addressed. Electronic mail: huanghb@ustc.edu.cn. URL: <http://staff.ustc.edu.cn/~huanghb>

solved. The LBM is an explicit scheme and the code is easy to parallelize. Ding and Aidun used a LBM to predict the critical Reynolds number when the 2D elliptical cylinder stops rotating in planar Couette flow.¹¹ The critical Re was confirmed by Zettner and Yoda through an experiment.¹⁴ Qi and Luo studied a prolate and an oblate particulate suspension in a 3D Couette flow by LBM.¹⁵ They identified several rotational modes. These studies all demonstrate that the LBM is a powerful tool to study particulate movement in fluids.

Using the LBM, Xia *et al.* studied the sedimentation of non-neutrally buoyant elliptical particle in a 2D channel with different block ratios at intermediate Re .¹² They found five different modes: the oscillatory mode, the “anomalous” rolling mode, the vertical mode, the inclined mode, and the horizontal mode. For the anomalous mode, the elliptical particle rotates as if it was contacting and rolling up one of the walls when it travels down vertically. However, significant differences may exist between 2D and 3D simulations.¹⁶

On the other hand, Swaminathan *et al.* have carried out 3D studies on the sedimentation of an ellipsoid inside an circular infinitely long tube at low and intermediate Re .⁹ In the study, the oscillatory and inclined modes are found. However, in their simulations, the tube diameter is fixed to be eight times the lengths of semi-major axis of the ellipsoid. The effect of the tube diameter on the motion behaviour of the particle is unknown. Whether the other three motion modes found in 2D simulations (the anomalous mode, the vertical mode, and the horizontal mode) will occur in 3D simulations is unknown. It is also unclear that under what circumstances, these modes may appear, i.e., the phase-diagram of these modes is unknown.

To better understand the effect of the tube wall and explore the motion mode under different circumstances, we here investigate the sedimentation of an ellipsoid in both narrow circular and square tubes for the Re up to 200. Description of the flow problem is give in Sec. II. In Sec. III, the LBM and the basic equations for the motion of the solid particle are introduced briefly. In Secs. IV A and IV B, the numerical method is validated. In Secs. V and VI, the results for circular and square tubes are presented, respectively. Conclusions are addressed in Sec. VII.

II. THE PROBLEM DESCRIPTION

The sedimentation of the ellipsoid in infinitely long tubes is illustrated in Figure 1. In the simulations of both cases, the computational domains all have dimension D , D , and L in the x , y , and z directions, respectively.

In this flow problem, there are 8 parameters that control the sedimentation of the spheroid: the tube width D , length of three semi-principal axes a ($a = \frac{A}{2}$), b , and c , density of the particle ρ_p , density of the fluid ρ_f , kinematic viscosity of the fluid ν , and gravity acceleration g . In our

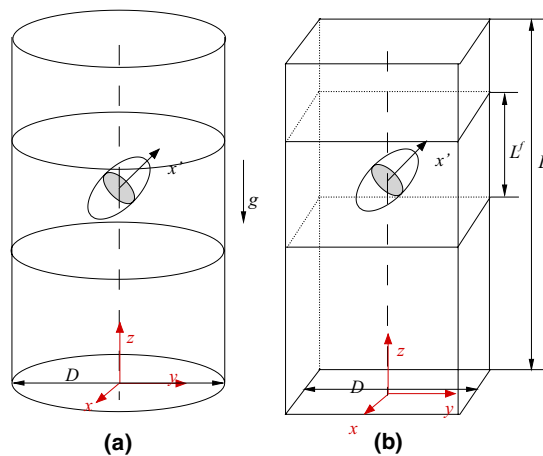


FIG. 1. Geometry of an ellipsoidal particle initially located at the center of (a) a circular tube and (b) a square tube. The particle is immersed and located in the center of the fine grid, which has dimension D , D , and L' in the x , y , and z directions, respectively.

study only cases with $b = c = \frac{a}{2}$ are considered. Hence, the non-dimensional parameters are: the non-dimensional width of the tube $\frac{D}{A}$, the density ratio $\frac{\Delta\rho}{\rho_f} = \frac{\rho_p - \rho_f}{\rho_f}$, and the Galileo number or ‘‘Archimedes number.’’¹⁷ The Galileo number is defined as^{17–20}

$$Ga = \sqrt{\frac{\Delta\rho}{\rho_f} \frac{ga^3}{v^2}}. \quad (1)$$

In our study,

$$\frac{ga^3}{v^2} = 1225 \quad (2)$$

is fixed, so $Ga^2 = 1225 \frac{\Delta\rho}{\rho_f}$; i.e., the density ratio and the Ga are not independent. Hence, there remain two non-dimensional parameters: $\frac{D}{A}$ and Ga (or $\frac{\Delta\rho}{\rho_f}$).

The Reynolds number in this problem is defined as $Re = \frac{U_t A}{\nu}$, where U_t is the average terminal velocity in the z -direction. As the velocity is unknown *a priori*, the Reynolds number is not a primary parameter. In the flow, Ga is a critical control parameter.

In all of our numerical tests, the velocity field is initialized as zero with a uniform pressure field ($p_0 = c_s^2 \rho_0$). The particle is released from the axis of the tubes $(0, 0, z_i)$ with zero velocity, where z_i is slightly larger than $\frac{L}{2}$. In our simulations, $L \approx 70a$ is adopted. The ellipsoid is always kept at a distance of approximately $35a$ from the two ends of the computational domain at all times (the technique is introduced in Sec. III E) so as to minimize the end effects.

The orientation of the ellipsoid particle and the boundary conditions are described in Secs. III B and III C, respectively.

III. NUMERICAL METHOD

The numerical method used in our study is based on the LBM.^{11,21–23} In the present study, the fluid flow is solved by the Multi-Relaxation-Time (MRT) LBM proposed by Lallemand and Luo²⁴ while the translational and orientational motions of the spheroid are modeled by the Newtonian and Euler equations, respectively.

A. MRT lattice Boltzmann equation

The MRT-LBM is able to recover the incompressible Navier-Stokes equation macroscopically.^{24,25} There are only two main steps in the code: streaming and collision. For the collision step,²⁵

$$|f^+(\mathbf{x}, t)\rangle = |f(\mathbf{x}, t)\rangle - M^{-1} \hat{\mathbf{S}} [|m(\mathbf{x}, \mathbf{t})\rangle - |m^{(eq)}(\mathbf{x}, \mathbf{t})\rangle], \quad (3)$$

and in the streaming step, distribution functions (DF) $|f(\mathbf{x}, t)\rangle$ in different directions (along \mathbf{e}_i) at each computational node propagate to their neighbourhood:

$$|f(\mathbf{x} + \mathbf{e}_i \Delta t, t + \Delta t)\rangle = |f^+(\mathbf{x}, t)\rangle, \quad (4)$$

where the Dirac notation of ket $|\cdot\rangle$ vectors symbolize the column vectors. In our 3D simulations, the D3Q19 velocity model is used¹³ and the discrete velocities \mathbf{e}_i are shown in Figure 2(a).

The collision matrix $\hat{\mathbf{S}} = M \cdot S \cdot M^{-1}$ is diagonal with $\hat{\mathbf{S}}^{25}$
 $\hat{\mathbf{S}} \equiv \text{diag}(0, s_1, s_2, 0, s_4, 0, s_4, 0, s_4, s_9, s_{10}, s_9, s_{10}, s_{13}, s_{13}, s_{13}, s_{16}, s_{16}, s_{16})$. $|m^{(eq)}\rangle$ is the equilibrium value of the moment $|m\rangle$. The 19×19 matrix M is a linear transformation which is used to map a vector $|f\rangle$ in discrete velocity space to a vector $|m\rangle$ in moment space, i.e., $|m\rangle = M \cdot |f\rangle$, $|f\rangle = M^{-1} \cdot |m\rangle$. The matrix M and $|m^{(eq)}\rangle$ are all identical to those used in Refs. 13 and 25.

The macro-variables density ρ and momentum j_ζ are obtained from

$$\rho = \sum_i f_i, \quad j_\zeta = \sum_i f_i e_{i\zeta}, \quad (5)$$

where ζ denotes x, y , or z coordinates. In our simulations, the parameters are chosen as: $s_1 = 1.19$, $s_2 = s_{10} = 1.4$, $s_4 = 1.2$, $s_9 = \frac{1}{\tau}$, $s_{13} = s_9$, and $s_{16} = 1.98$. The parameter τ is related to the kinematic

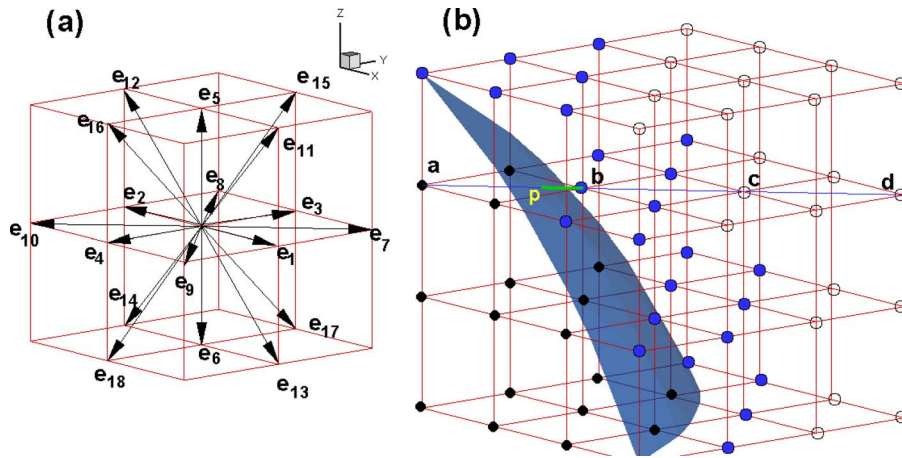


FIG. 2. (a) D3Q19 velocity model, e_1 to e_{18} represent 18 non-zero components and e_0 is a zero component and not labeled; (b) illustration of “interpolation bounce-back.” The black filled circles are solid nodes, which are inside the surface of the solid body. The other circles are fluid nodes and the gray filled circles (blue) denote the fluid nodes which have at least one link with solid nodes (any of the 18 directions).

viscosity of the fluid with $\nu_f = c_s^2(\tau - 0.5)\Delta t$ and $c_s = \frac{c}{\sqrt{3}}$, where $c = \frac{\Delta x}{\Delta t}$ is the lattice speed, where Δx and Δt are the lattice spacing and time step in LB simulations, respectively. The pressure in the flow field can be obtained from $p = c_s^2\rho$.

B. Rotation and translation of the particle

As shown in Figure 3, the ellipsoid in our study is described by

$$\frac{x'^2}{a^2} + \frac{y'^2}{b^2} + \frac{z'^2}{c^2} = 1, \tag{6}$$

where (x', y', z') represents the body-fixed coordinate system and $a, b,$ and c are the radii of three semi-principal axes in $x', y',$ and z' -direction, respectively. The length of the major axis of the ellipsoid is $A = 2a$. As shown in Figure 3, the spatial orientation of any body-fixed frame (coordinate system) can be obtained by a composition of rotations around $z'-x'-z'$ -axis with Euler angles (φ, θ, ψ) from the space-fixed frame (x, y, z) that initially overlaps the body-fixed frame.¹³ $\alpha, \beta,$ and γ are used to denote the angles between the x' -axis and the space fixed coordinates $x, y,$ and z -axis, respectively, with $\cos^2\alpha + \cos^2\beta + \cos^2\gamma = 1$.

The translational velocity $\mathbf{U}(t)$ of the solid particle is determined by solving Newton’s equation.¹³ The rotation of the spheroid is determined by Euler equations, which are written as

$$\mathbf{I} \cdot \frac{d\boldsymbol{\Omega}(t)}{dt} + \boldsymbol{\Omega}(t) \times [\mathbf{I} \cdot \boldsymbol{\Omega}(t)] = \mathbf{T}(t), \tag{7}$$

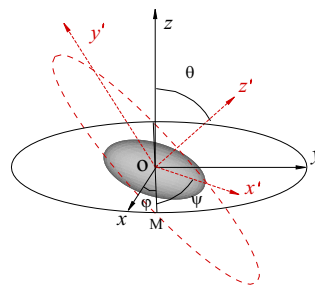


FIG. 3. Schematic diagram of a spheroid with its symmetry axis in x' -direction in fluid. (x, y, z) and (x', y', z') represent the space-fixed frame and the body-fixed coordinate system, respectively. Line “OM” represents the intersection of the (x, y) and the (x', y') coordinate planes.

where \mathbf{I} is the inertial tensor. In the body-fixed coordinate system, the tensor is diagonal¹³ and the principal moments of inertia are $I_{x'x'} = m \frac{b^2+c^2}{5}$, $I_{y'y'} = m \frac{a^2+c^2}{5}$, and $I_{z'z'} = m \frac{a^2+b^2}{5}$, where $m = \rho_p \frac{4}{3} \pi abc$ is the mass of the suspended particle. $\boldsymbol{\Omega}$ represents angular velocity and \mathbf{T} is the torque exerted on the solid particle in the same coordinate system. Here four quaternion parameters¹⁵ are used as generalized coordinates to solve the corresponding system of equations. With the quaternion formulation, $\boldsymbol{\Omega}$ in (7) can be solved using a fourth-order accurate Runge-Kutta integration procedure.¹³

C. Boundary conditions

As we know, the no-slip boundary condition should be ensured in the particle's surface and the tube wall. Here, the fluid-solid coupling in our study is based on the schemes of Refs. 23 and 24.

In Figure 2(b), the computational domain was separated by a solid surface. Some lattice nodes which inside the surface are solid nodes (filled black circles) and the collision steps are not implemented in these nodes. Outside the surface, there are fluid nodes, which are represented by the gray filled circles (blue) and black circles. The gray filled circle (blue) denotes the fluid nodes which have at least one link of the 18 directions (shown in Figure 2(a)) connecting with the solid nodes. Usually the half-way bounce back is used^{21,23} to ensure the no-slip boundary condition. In Figure 2(b), we can see that after streaming step, there are 6 directions unknown for the lattice node \mathbf{b} , i.e., $f_1(\mathbf{b})$, $f_3(\mathbf{b})$, $f_5(\mathbf{b})$, $f_7(\mathbf{b})$, $f_{15}(\mathbf{b})$, $f_{11}(\mathbf{b})$. For the half-way bounce back scheme (or simple bounce back), the unknown DF that comes from the solid node is set to be the DF in the reverse direction, which is already known. For example, $f_1(\mathbf{b}) = f_2(\mathbf{b})$.

Here a more accurate curve wall boundary condition^{24,26} is applied. In the following, an example about how to get $f_7(\mathbf{b})$ is illustrated in detail and the other DFs can be obtained in the similar way. In Figure 2(b), suppose the line \mathbf{ab} intersects with the solid surface at point \mathbf{p} . $|\mathbf{bp}|$ denotes the length of the green line \mathbf{bp} . Here a parameter $q = \frac{|\mathbf{bp}|}{|\mathbf{ab}|}$ is defined to describe the fraction in fluid region of a grid spacing intersected by the solid surface. After the streaming step, the unknown $f_7(\mathbf{b})$ can be obtained through a second-order interpolation from the surrounding points.²⁴ For example, if $q < \frac{1}{2}$, $f_7(\mathbf{b}) = q(1 + 2q)f_{10}(\mathbf{a}) + (1 - 4q^2)f_{10}(\mathbf{b}) - q(1 - 2q)f_{10}(\mathbf{c})$. If the solid surface is moving with velocity \mathbf{u}_w , then an extra term $w_i \rho_f \frac{\mathbf{e}_7 \cdot \mathbf{u}_w}{c_s^2}$ should be added to $f_7(\mathbf{b})$, which takes account of the moving wall. Here $w_0 = \frac{1}{3}$, $w_i = \frac{1}{18}$ for $i = 1, 2, \dots, 6$, and $w_i = \frac{1}{36}$ for $i = 7, 8, \dots, 18$. More details about the "interpolation bounce back" can be found in Ref. 24.

The force on solid boundary nodes is calculated through the momentum exchange scheme^{24,27} and the force due to the fluid particle entering and leaving the solid region²³ is also considered.

For the boundary conditions, the zero velocity boundary condition is applied at the bottom inlet boundary.¹³ For the upper outlet boundary condition, the constant pressure boundary condition is applied, where the velocity is extrapolated from the inner fluid nodes.¹³

D. Interaction between wall-particle

When the distance between the particle and the wall is small enough, some repulsive force models, such as the spring force model²⁸ and the lubrication force model²⁹ are used to prevent overlapping. The repulsive force is important and it is physical because it mimics the force due to the collision between solid surfaces. For the above two models, in terms of results, there are almost no discrepancy between them.¹² Here, we have used the spring force model, i.e., the repulsive force

$$\mathbf{F}_R = \begin{cases} 0, & \text{if } |\mathbf{x}_s| > s, \\ \frac{C}{\varepsilon_w} \left(\frac{|\mathbf{x}_s| - s}{s} \right)^2 \frac{\mathbf{x}_s}{|\mathbf{x}_s|}, & \text{if } |\mathbf{x}_s| < s, \end{cases} \quad (8)$$

where s is the threshold distance, ε_w is the stiffness parameter, $C = \frac{4}{3} \pi abc (\rho_p - \rho_f) g$ is the force scale with g the gravity acceleration, and \mathbf{x}_s denotes the vector from the point on the wall which is closest to the ellipsoid to the corresponding point on the ellipsoid.

To validate our LBM code, the lubrication force formula²⁹ is also used for comparison. The original formula is proposed for two spheres with radii of R_a and R_b ,²⁹

$$\mathbf{F}_L = \begin{cases} 0, & \lambda > s, \\ -6\pi\rho\nu\frac{R_a^2R_b^2}{(R_a+R_b)^2}\left(\frac{1}{\lambda}-\frac{1}{s}\right)(v_a-v_b)\frac{\mathbf{x}_a-\mathbf{x}_b}{|\mathbf{x}_a-\mathbf{x}_b|}, & \lambda \leq s, \end{cases} \quad (9)$$

where \mathbf{x}_a and \mathbf{x}_b denote the central positions of the spheres, v_a and v_b are their velocities along the vector $(\mathbf{x}_b - \mathbf{x}_a)$. λ and s are the gap between the spheres and the threshold distance. Here for the ellipsoidal particle, in this formula $R_a = R_b = a$ is adopted. \mathbf{x}_a and \mathbf{x}_b denote the point on the ellipsoid which is closest to the tube wall and the corresponding point on the tube wall, respectively. v_a is the velocity at \mathbf{x}_a along the vector $(\mathbf{x}_b - \mathbf{x}_a)$, and $v_b = 0$.

E. Dynamic multi-block strategy in simulations

To calculate the force acting on the spheroid more accurately, grid refinement is used near the particle. As shown in Figure 1, in our simulations, usually the fine grid has dimension D , D , and L^f in the x , y , and z directions, respectively, and is located in the middle of the computational domain. The particle is immersed and located in the center of the fine grid. L^f is usually taken as $3a$.

The coupling scheme between the fine and coarse grids is essentially identical to the multi-block scheme.³⁰ The only difference is that in our simulations, the refined grid may travel with the ellipsoid¹² and the top and the bottom layers in the coarse grid may be “removed” and “added,” respectively. Here, $1\ lu$ and $1\ ts$ are used to denote 1 lattice unit (Δx_f) and 1 time step (Δt_f) in fine grid, respectively. The rest of the computational domain is filled with coarse mesh and the lattice spacing $\Delta x_c = 2\ lu$ and $\Delta t_c = 2\ ts$. Suppose τ_f and τ_c are the relaxation times in the fine mesh and coarse mesh, respectively. Due to viscosity consistency, they satisfy the formula $\nu = c_s^2(\tau_f - 0.5)\Delta t_f = c_s^2(\tau_c - 0.5)\Delta t_c$.³⁰

The vertical position of the ellipsoid z is always kept approximately $\frac{L}{2}$ in the tube for all time so as to minimize the end-effects. If $z > \frac{L}{2} + \Delta x_c$, suppose initially the top and bottom of the fine grid are overlap with the k_1 , and k_2 horizontal layers of the coarse grid ($k_1 > k_2$), where k_1, k_2 are the vertical indices of the coarse grid. After several time steps, the particle may sediment a vertical lattice unit Δx_c inside the fine grid, the fine grid should shift, i.e., “adding” and “removing” two layers in the bottom and top of the fine grid, respectively, because $\Delta x_c = 2\Delta x_f$. In the implementation, the top and bottom of the fine grid become overlap with the $k_1 - 1$, and $k_2 - 1$ layers of the coarse grid.

On the other hand, once $z < \frac{L}{2}$, we have to “add” and “remove” one layers (Δx_c) in the bottom and top of the coarse grid, respectively. In this way, it seems that the particle “moves” Δx_c upward hence the vertical distance between the center of the ellipsoid and the new bottom layer, i.e., the updated z , is still kept larger than $\frac{L}{2}$. In the implementation, the data of the macro-variables and distribution functions in the coarse grid should “move” upward one layer (Δx_c).³¹

To make the simulations more efficient, a parallel code based on Message Passing Interface (MPI) is compiled. In the parallel code, the coarse grid is divided into several sections vertically; it means that they are assigned to several Central Processing Units (CPUs) and an extra CPU is in charge of the fine grid.

IV. VALIDATION

A. Validation I: Migration of a sphere in Poiseuille flows

To validate our LBM code, the migrations of a neutrally buoyant sphere in tube Poiseuille flows were studied. As we know, many experiments about the migration of spheres, rods, and disks in Poiseuille flows were carried out extensively.^{2,32} Here, our LBM results are compared with those obtained in experiments.²

In our simulations, $y = 0$ is the tube axis and $\frac{y}{R} = 1$ is the wall. The radii of the tube and the sphere are $R = 0.2\ \text{cm}$ and $r = 0.061\ \text{cm}$, respectively. The sphere is initially put in the (y, z) -plane. Two cases with initial positions $y/R = 0.21$ and 0.68 were simulated. The density of

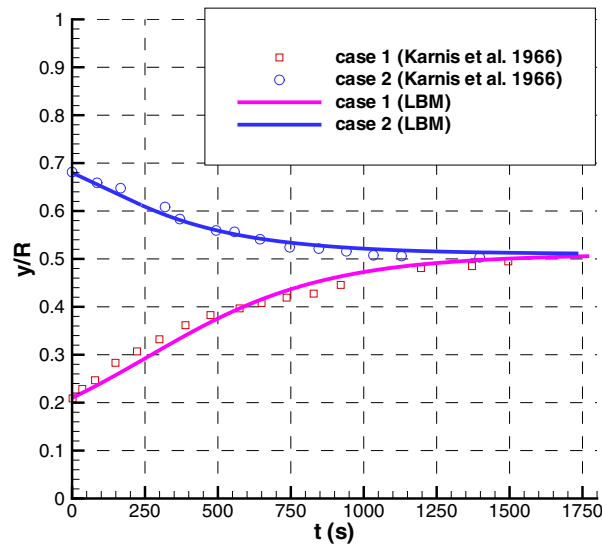


FIG. 4. Migration trajectories of a neutrally buoyant sphere in Poiseuille flows. Two cases with different initial positions were simulated and compared with experimental data.² The spheres are put in the (y, z) -plane and released from $\frac{y}{R} = 0.21$ (case 1) and $\frac{y}{R} = 0.68$ (case 2), respectively.

the fluid is 1.05 g/cm^3 and $\mu = \rho\nu = 1.2 \text{ g/cm s}$. The flow rate is $Q = 7.11 \times 10^{-2} \text{ cm}^3/\text{s}$. Because $Q = \frac{\pi R^2}{2} U_m$, the corresponding $Re = \frac{U_m R}{\nu} = 0.198$, where U_m is the maximum velocity in the axis of the tube.

To make the simulations more efficient, the multi-block strategy is also used. The fine mesh size is $68 \times 68 \times 40$, the coarse mesh size is $34 \times 34 \times 120$, and tube length is $L = 240 \text{ lu}$. In the simulations, the relaxation times are set as $\tau_f = 0.9$, $\tau_c = 0.7$. The radius of the tube is $R = 29.5 \text{ lu}$. To match the Re , in our simulation $U_m = 8.97 \times 10^{-4} \text{ lu/ts}$ and the corresponding pressure drop between the inlet and outlet is $\Delta p = 1.32 \times 10^{-4} \text{ mu/lu ts}^2$, where mu means *mass unit*. In the simulations $1 \text{ lu} = 0.00678 \text{ cm}$, $1 \text{ ts} = 5.36244 \times 10^{-6} \text{ s}$, $1 \text{ mu} = 3.272 \times 10^{-7} \text{ g}$.

The trajectories of spheres released from the $\frac{y}{R} = 0.21$ (case 1) and $\frac{y}{R} = 0.68$ (case 2) and those measured in Ref. 2 are illustrated in Figure 4. It is shown that the LBM results are in excellent agreement with the experimental ones. The approach to an equilibrium position roughly midway between the center and the wall is the well-known Segre-Silberberg effect.

B. Validation II: Sedimentation of an ellipsoid

To further validate our simulation, an ellipsoid sedimentation in a circular tube is simulated and compared with the cases in Ref. 9. In the simulations, the density of the fluid is 1.0 g/cm^3 . The gravity is $g = 980 \text{ cm/s}^2$, the viscosity of the fluid $\nu = 0.01 \text{ cm}^2/\text{s}$, tube diameter $D = 0.4 \text{ cm}$. In our LBM simulation, $\frac{\Delta\rho}{\rho_f} = 0.01$, the length of the major axis of the ellipsoid $A = 0.1 \text{ cm}$ is represented by 52 lu , which means $1 \text{ lu} = 0.001923 \text{ cm}$. The density of fluid is set to be $\rho_f = 1 \text{ mu/lu}^3$ and $1 \text{ mu} = 7.112 \times 10^{-9} \text{ g}$. In this particular case $\tau_f = 1.2$. Hence, 1 ts represents $8.63 \times 10^{-5} \text{ s}$.

The initial orientation of the particle is $(\phi_0, \theta_0, \psi_0) = (90^\circ, 90^\circ, 45^\circ)$, which means the evolution axis is in the (y, z) -plane and angle between x' axis and x axis is 45° . The other parameters are $\varepsilon_w = 0.0025$, $s = 2 \text{ lu}$. The coarse mesh is $108 \times 108 \times 900$; the fine mesh is $56 \times 212 \times 86$. Noted that $\Delta x_c = 2\Delta x_f$ so the dimension of the coarse mesh is $216 \text{ lu} \times 216 \text{ lu} \times 1800 \text{ lu}$ and the length of the tube is about $L \approx 70a$. The particle is kept in the center of the domain using the dynamic multi-block strategy.

The results for comparison are shown in Figure 5. y^* , z^* are the normalized positions in y -axis and $-z$ -direction (normalized by $D/2$). It is noted that Ga while not Re is a true control parameter of the flow. However, Ga is not given in Ref. 9. For comparison purpose, we have to try different $\frac{\Delta\rho}{\rho_f}$

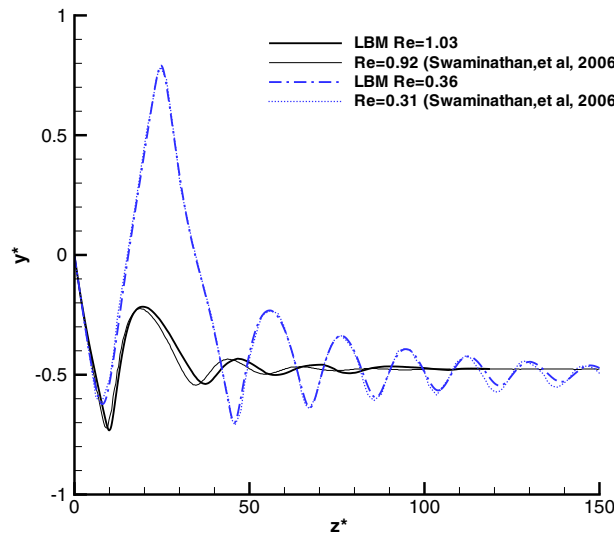


FIG. 5. Trajectory of the center of ellipsoids when they sediment in a circular tube at various Reynolds number. The centers of the ellipsoids are initially put in the axis of the tube, with x' -axis inside the (y, z) -plane. The initial orientations are $\gamma = 45^\circ$. y^* , z^* are the normalized positions in y -axis and $-z$ -direction (normalized by $D/2$).

to make the simulated Res close to the Res in their cases.⁹ Here the cases of $Ga = 3.43, 9.78$ are simulated, which have $Re = 0.36$ and 1.03 , respectively.

For the case of $Re \approx 0.31$, our result ($Re = 0.36$) agrees well with that in Ref. 9. In this case, the particle moves and rotates inside the (y, z) -plane. It is seen that at $z^* \approx 15$, it moves across the axis. At $z^* \approx 25$, the ellipsoid collides with the wall and then moves towards the axis of the tube. After it passes through the z -axis again, the spheroid enters the inclined mode (settling off-axis with a constant inclination to the horizontal). The trajectory of the oscillatory movement in our simulation is well consistent with the prediction in Ref. 9. This case also demonstrates the spring force model used in our scheme is effective and the choices of $\epsilon_w = 0.0025$, $s = 2$ lu are reliable.

In the case of $Re \approx 1.0$, both trajectories (“LBM $Re = 1.03$ ” and “ $Re = 0.92$ ”⁹) oscillate for a while and finally reach an almost identical equilibrium y -position. Our LBM simulations are consistent with the data in Ref. 9.

The grid independence and time-step independence studies are also carried out. It is found that $\Delta x_f = 0.00385$ cm and $\Delta t_f = 0.0000986$ s are small enough to get accurate result for the above case $Ga = 3.43$ (the result is not shown here for brevity). In the following study, $\Delta x_f = 0.001923$ cm and $\Delta t_f = 0.0000986$ s are adopted.

The effect of the repulsive models on our numerical result is also tested. Cases of an oscillatory sedimentation inside a circular tube were simulated to investigate the effect. In the cases, the density ratio $\frac{\rho_p}{\rho_f} = 1.4$ ($Ga = 22.1$); the tube diameter is $D = \frac{12}{13}A$, and $A = 52$ lu. The initial orientation of the particle is set as $(\varphi_0, \theta_0, \psi_0) = (90^\circ, 90^\circ, 60^\circ)$. The parameters for the repulsive force models are listed in Table I.

From Figure 6, we can see that for case 1 and case 2, although ϵ_w is different (s is fixed to be 2 lu), the trajectories collapse into one curve. Hence, the result is not sensitive to the value of ϵ_w . From

TABLE I. Parameters for the repulsive force models (oscillatory mode).

Case	ϵ_w	s (Δx_f)	Repulsive model
Case 1	0.0025	2	Spring force (Eq. (8))
Case 2	0.25	2	Spring force (Eq. (8))
Case 3	0.0025	1	Spring force (Eq. (8))
Case 4	...	2	Lubrication force (Eq. (9))

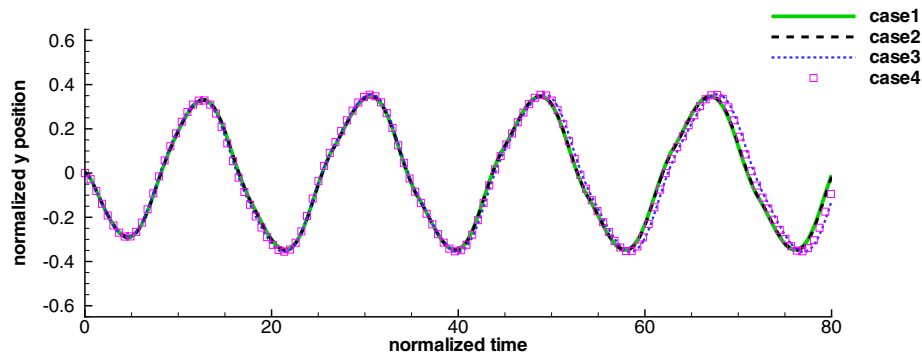


FIG. 6. Trajectories of four oscillatory cases (parameters listed in Table I) are compared.

the comparison between case 1 and case 3, we can see that the parameter $s = 2$ lu, or $s = 1$ lu does not affect the behaviour mode of the particle although there is a very small discrepancy between their trajectories (the period of case 3 is slightly larger than that of case 1 but the difference is less than 1.5%).

It is also seen that the trajectories of case 3 and case 4, which using the spring force and the lubrication force, respectively, agree very well. Hence, the results presented are almost independent of the detail of the repulsive modeling.

V. SEDIMENTATION OF AN ELLIPSOID INSIDE A CIRCULAR TUBE

Through many simulations with different D/A and density ratio (or Ga), we observed several modes of motion. Although usually the initial orientation of the particle is $(\varphi_0, \theta_0, \psi_0) = (90^\circ, 90^\circ, 60^\circ)$, we found that the modes are all independent of the initial orientation based on limited observation.

A. Modes in the circular tube

Figure 7 shows the snapshots of several typical modes in our simulations. The density ratio and $\frac{D}{A}$ in each case are also given in the caption. The results presented here are for the situation when the initial transient (which depends on the initial position and orientation) dies out, and the particle trajectory reaches steady state or time periodic solution.

As shown in Figure 7(a) for the spiral mode, the particle spirals around the axis of the tube. The x' -axis seems to rotate around the z -axis but the angle γ is almost a constant. In the (x, y) -plane, the projection of the trajectory of the spheroid center is a circle.

Figure 7(b) shows the oscillatory mode, the spheroid “wiggles” down the tube. When the particle approaches the left and right sides, it rotates counterclockwise and clockwise, respectively, due to the torque exerted by flow field.⁹ The direction of rotation in this mode is referred to as “reverse-contact” rolling,⁹ which means the particle rotates as if it is rolling up the side wall near the closest contact³³ when it is settling down. It is called “anomalous rotating” because it is obviously different from the behaviour of the particle when it contacts with the inclined wall under gravity without surrounding fluids (“normal rotating” or “regular rolling”).³³ This mode looks like leaves falling in air.¹⁸ However, leaves falling in air are different from the present mode because the object’s rolling direction is different.

Figure 7(c) shows the inclined mode. The particle may settle off-axis with a constant inclination to the horizontal and the x' -axis is inside an axisymmetric plane. The orientation is very close to horizontal orientation in tubes with $\frac{D}{A} > 1$. When $\frac{D}{A} < 1$, the inclined mode may also appear but the orientation is close to a vertical state due to confinement of the tube (vertically inclined). When the ellipsoid sediments under the inclined mode, it may also collide with the wall simultaneously (Figure 7(d)). That means the particle settles down under inclined mode with oscillations (inclined mode II).

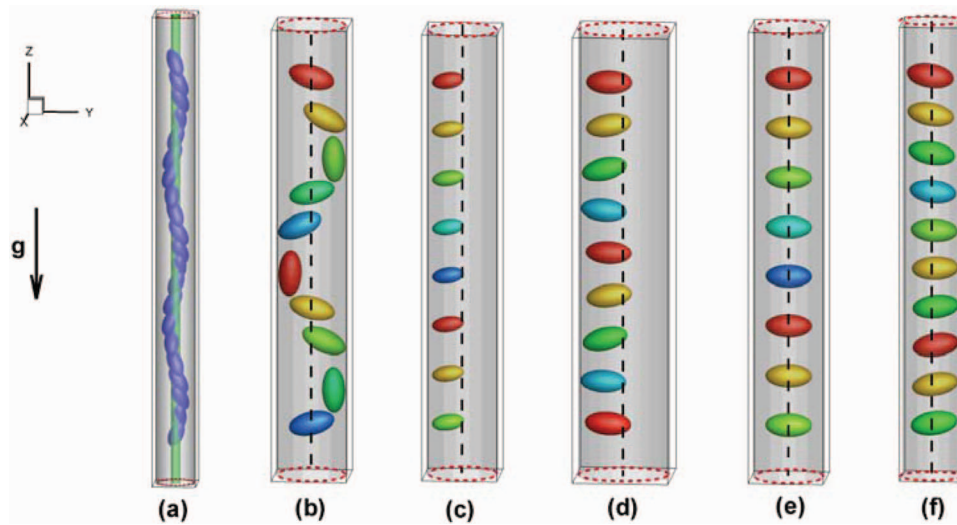


FIG. 7. Snapshots of typical modes. (a) Spiral mode ($\frac{D}{A} = \frac{12}{13}$, $Ga = 70.0$), the particle settles spirally, the inner circular tube (green) with radius r is drawn to guide the eye. (b) Oscillatory mode ($\frac{D}{A} = \frac{16}{13}$, $Ga = 9.9$), trajectory of the ellipsoid is always inside an axis symmetric plane; (c) inclined mode ($\frac{D}{A} = \frac{5}{2}$, $Ga = 7.0$), the ellipsoid settles off-axis with a constant inclination to the horizontal; (d) inclined mode II (with oscillation, $\frac{D}{A} = 2$, $Ga = 6.1$); (e) horizontal mode ($\frac{D}{A} = \frac{20}{13}$, $Ga = 35.0$); (f) horizontal mode II (with oscillation, $\frac{D}{A} = \frac{16}{13}$, $Ga = 55.3$). Different colors shown in (a)–(f) represent the spheroid position at different time. The dashed vertical lines in (a)–(f) denote the axes of the circular tubes.

Figure 7(e) shows the horizontal mode. The sedimentation is symmetric with respect to the tube axis. For higher Re , due to periodic hydrodynamic force, as shown in Figure 7(f), the particle may also sediment symmetrically with oscillation (horizontal mode II).

In the following, the characteristics of the spiral and vertically inclined mode will be described in detail.

B. Spiral mode and vertically inclined mode

The spiral mode and vertically inclined mode only appear when $\frac{D}{A} < 1$, i.e., the diameter of the tube is less than the major axis of the ellipsoid. For the spiral mode, the position, orientation, and velocities as functions of normalized time are shown in Figure 8. The length, time, and velocities are normalized by $\frac{D}{2}$, $\sqrt{A/g}$, and \sqrt{gA} , respectively. In Figure 8(a), the radial distance between the center of the ellipsoid and axis of tube, i.e., $r = \sqrt{x^2 + y^2}$, is also shown. It is almost a constant. Hence, in the (x, y) -plane, the projection of the trajectory of the spheroid center is a circle. In this mode, the angle between x' and z , i.e., γ , is almost a constant. From Figure 8(c), it is seen that in this mode the sedimentation velocity is almost a constant.

It is noted that the period of the spiral mode is smaller than that in the oscillatory mode. For example, the normalized periods of cases $\frac{D}{A} = \frac{12}{13}$, $Ga = 35.0$ (oscillatory mode), and $Ga = 70.0$ (spiral mode) are 7.84 and 2.05, respectively.

When Ga is higher, the vertically inclined mode may appear. The position and orientation as functions of normalized time in the case of $\frac{\Delta\rho}{\rho_f} = 17$ ($Ga = 144.3$) are shown in Figure 9. The position of the particle and the orientation all reach constant values after the normalized time $t^* = 53$, indicating that the ellipsoid enters the equilibrium state. The snapshot of the particle is shown in Figure 9(c). It is noted that when the particle enters the periodic spiral mode or the steady vertically inclined mode, the ellipsoid will not contact with the wall of the tube any more.

C. Phase diagram of D/A - Ga

Figure 10 shows the mode distribution in the $(D/A, Ga)$ -plane. It is identified that there exist several regions for $D > A$. The oscillatory mode usually occurs in the lower Ga region. At higher Ga ,

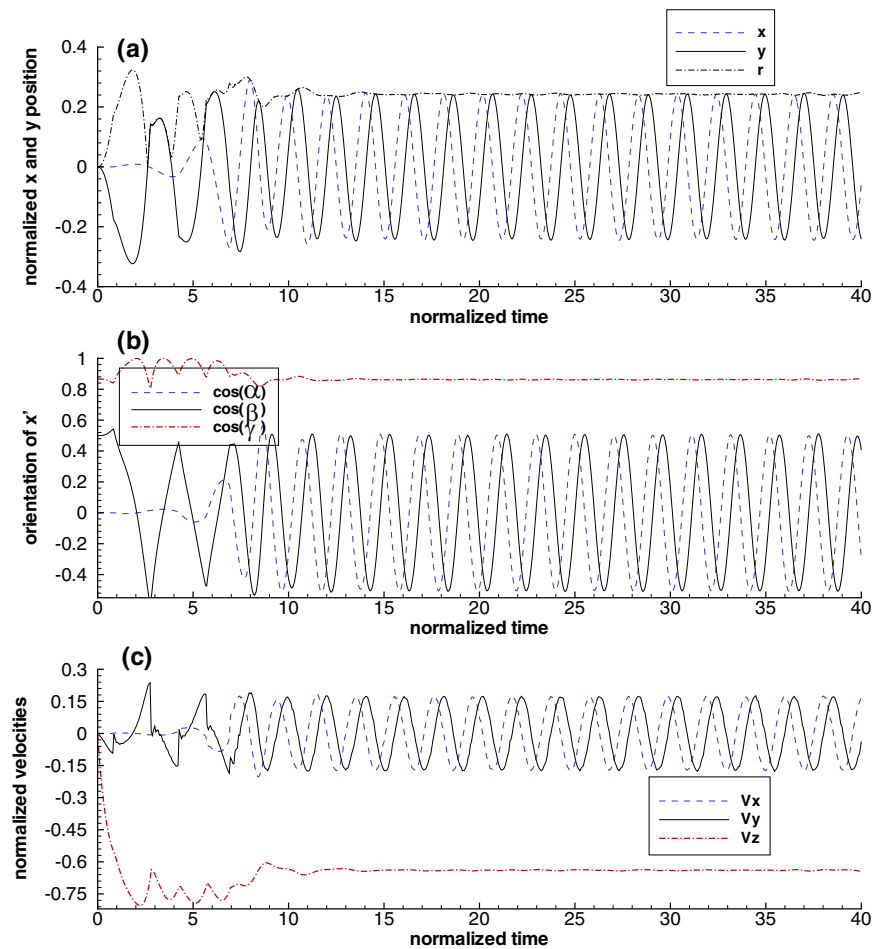


FIG. 8. Spiral mode when an ellipsoid settles in a circular tube ($\frac{D}{A} = \frac{12}{13}$, $Ga = 70.0$). (a) The normalized x and y positions of the center of ellipsoid, (b) the orientation of the x' -axis, and (c) the velocities (V_x , V_y , V_z) of the ellipsoid as functions of time.

the horizontal mode, in which the ellipsoid sediments along the axis, is dominant. Horizontal mode II may occur at $Ga \sim O(10^2)$ and in narrow tubes ($\frac{D}{A} \sim 1.2$). At an intermediate Ga , the inclined mode appears. Inclined mode II approximately occurs on the border between the oscillatory mode and the inclined mode, which means that it appears at relatively lower Ga than the normal inclined mode. For $D < A$, besides the oscillatory mode in lower Ga , the spiral mode and the vertically inclined mode occurs at higher Ga ($\frac{D}{A} = \frac{12}{13}$, $\frac{\Delta\rho}{\rho_f} > 8.0$). In this inclined mode, the x' -axis is almost vertical.

The Re as a function of $\frac{\Delta\rho}{\rho_f}$ (or $\frac{Ga^2}{1225}$) for circular tubes is shown in Figure 11. At lower Re , the flow is dominated by viscous effect and $Re \approx Ga^2$ (i.e., $Re \approx \frac{\Delta\rho}{\rho_f}$). At higher Re , the flow is dominated by inertial effect, $Re \approx Ga$ (i.e., $Re \approx (\frac{\Delta\rho}{\rho_f})^{\frac{1}{2}}$).

Figure 10 shows that there is a small overlap region for cases of $\frac{D}{A} = \frac{16}{13}$ at $Re \approx 30$ although the overlap region is limited in a very small region. The smaller region means that the lighter ellipsoid (a lower $\frac{\Delta\rho}{\rho_f}$) settles in oscillatory mode faster than the heavier one in the inclined mode. That is also clearly shown in the curve of $\frac{D}{A} = \frac{16}{13}$ at $Re \approx 30$ in Figure 11(b). This can be explained as follows. In the inclined mode ($D > A$), the orientation of the particle is always almost horizontal, thus it experiences a relatively larger drag force coefficient. By contrast, in the oscillatory mode, its orientation changes periodically from vertical to almost-horizontal. When the orientation is close to the vertical state, it experiences a smaller drag force. Hence, the average drag force coefficient may

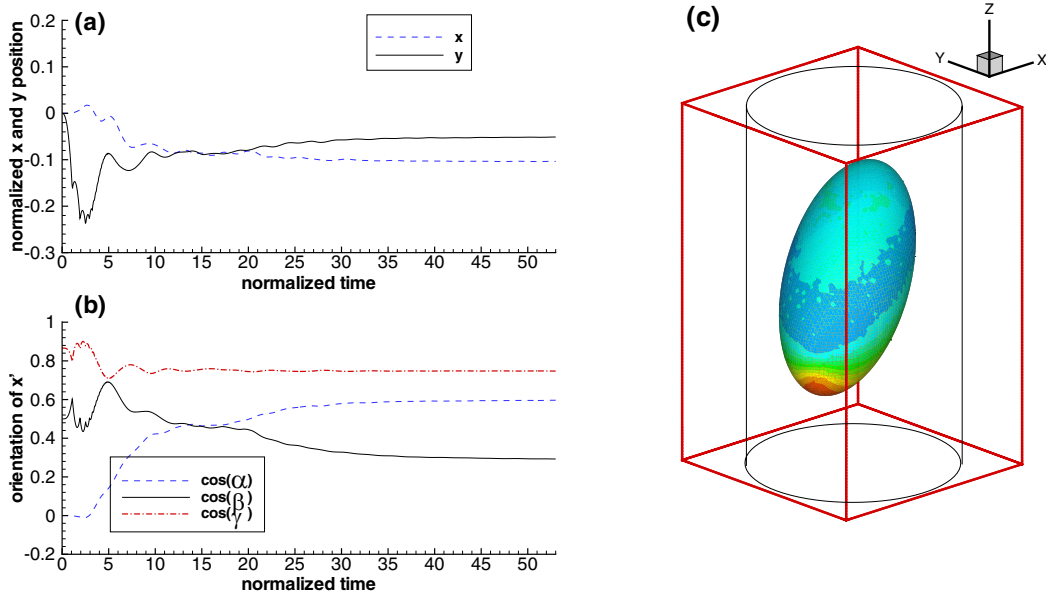


FIG. 9. Vertically inclined mode when an ellipsoid sediments in a circular tube ($\frac{D}{A} = \frac{12}{13}$, $Ga = 144.3$). (a) The normalized x and y positions of the center of ellipsoid, (b) the orientation of the x' -axis, (c) the snapshot of the ellipsoid in steady state, the contour of the pressure is drawn in the surface of the ellipsoid.

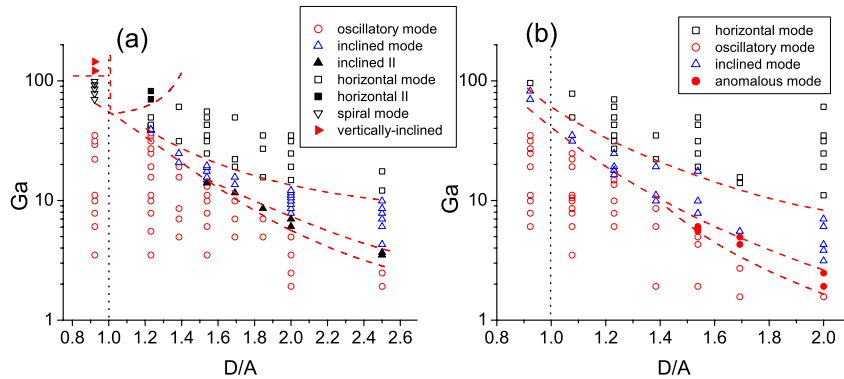


FIG. 10. Phase space of $D/A - Ga$ showing the regions leading to different modes. (a) Circular tubes and (b) square tubes. Black dot lines represent the cases $D = A$. The dashed lines (red) roughly mark the boundaries of different flow regimes.

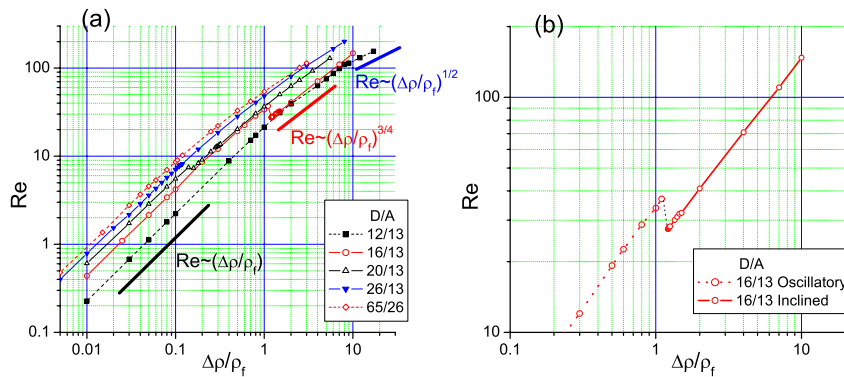


FIG. 11. (a) Terminal Re as a function of $\frac{\Delta\rho}{\rho_f}$ (or $\frac{Ga^2}{1225}$) and (b) zoom in view of cases $\frac{D}{A} = \frac{16}{13}$.

be smaller than that in the inclined mode; the average sediment velocity in the oscillatory mode is larger. Hence, a lighter particle settles faster than a heavier one in this tube.

VI. SEDIMENTATION OF AN ELLIPSOID INSIDE A SQUARE TUBE

A. Phase-diagram

The mode distribution for square tubes on the $(D/A, Ga)$ -plane is shown in Figure 10(b). It is seen that the mode distribution pattern for square tubes is similar to that for circular tubes but there are two significant differences between Figures 10(b) and 10(a). One is that a new mode: the anomalous rolling mode, occurs in cases of $\frac{D}{A} = \frac{20}{13}, \frac{22}{13},$ and $\frac{26}{13}$ and $Ga \sim O(1)$. The anomalous rolling mode seems to be a transitional mode between the oscillatory mode and the inclined mode. It occurs when the tube width $\frac{D}{A} \geq \frac{20}{13}$ and $Ga \sim O(1)$. The other is that in all these modes, the ellipsoid eventually moves in a specific plane, i.e., the diagonal plane of the square tube. The diagonal plane seems to be globally stable. The anomalous rolling mode was also observed in 2D study of elliptical particle sedimentation inside a channel.¹² However, as far as we know, no one has reported it in 3D simulations before. In the following, we will discuss the mode in detail.

B. Anomalous mode

From the phase diagram, it is observed that the anomalous mode occurs in square tubes with $\frac{20}{13} \leq \frac{D}{A} \leq 2$ and $Ga \sim O(1)$. For narrower tubes, no such mode exists.

To illustrate the motion of the ellipsoid clearly, snapshots of eight different orientations during one period are shown in Figure 12. The contours of the pressure are also drawn on the surface of the particle. The bottom and the upper of the particle experience higher and lower pressure, respectively. The ellipsoid is contacting the front left corner and rolling counterclockwise as it settles down. The ellipsoid periodically contacts one corner and then approaches but does not move across the z -axis. The ellipsoid always only rotates in one direction (clockwise or counterclockwise).

The position and the orientation of the ellipsoid and the torque acting on the ellipsoid are shown in Figures 13(a) and 13(b), respectively. The labels “a” to “h” denote the eight snapshots at different times in Figure 12. The particle experiences a periodic torque which makes it tumble periodically. At point “a,” the ellipsoid is almost horizontal. After point “a,” the particle approaches the front left corner, before $t = 4000$, the particle experiences a positive torque which makes it rotate counterclockwise. After $t = 4000$, a small negative torque acts on the particle, which may be related to

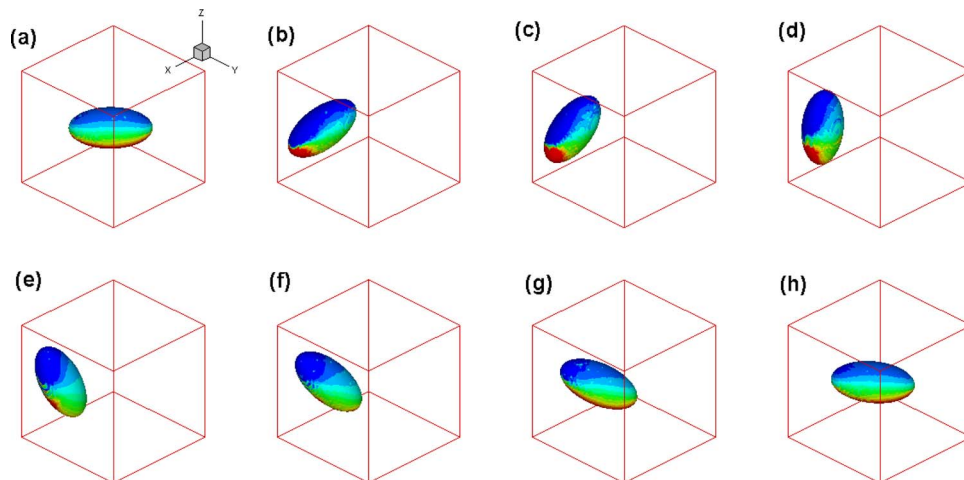


FIG. 12. Anomalous mode in a square tube ($\frac{D}{A} = \frac{20}{13}, \frac{\Delta\rho}{\rho_f} = 0.03$). The evolution axis of the ellipsoid (x') is always inside the diagonal plane of the tube. Eight snapshots at different time in a period are shown in (a)–(h). From (a) to (h), the corresponding normalized times are 3858, 4078, 4102, 4127, 4151, 4176, 4200, and 4249, respectively (refer to Figure 13).

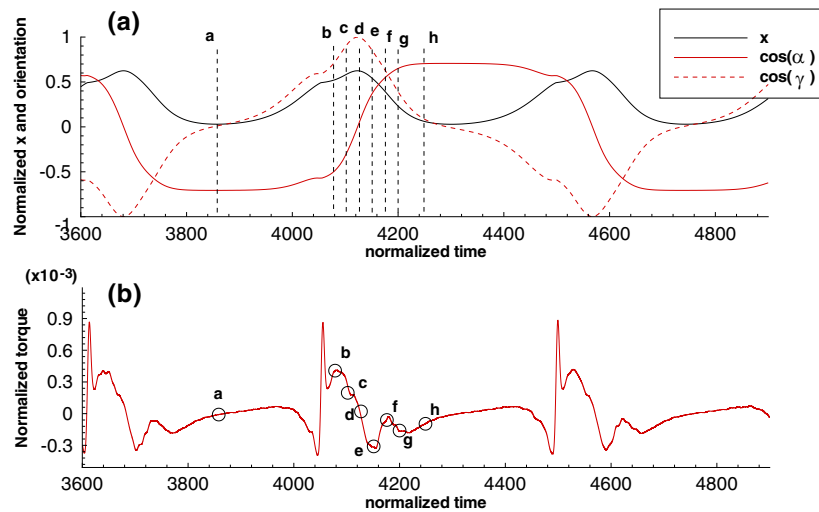


FIG. 13. Anomalous mode in a square tube (case in Figure 12). (a) The normalized x and orientation of ellipsoid and (b) the torque acting on the ellipsoid as a function of time. The torque is in the direction (1, 1, 0) in the space fixed coordinates and normalized by $\frac{4}{3}\pi abc(\rho_p - \rho_f)ga$.

the shear stress force acting on the particle. At $t \approx 4050$ (point “b”), the gap between the particle and the walls is close enough and the repulsive force is activated, which induces a large positive torque on the particle. Hence, there is a sharp increment in the torque curve at that time. After that, the ellipsoid becomes vertical gradually (from “b” to “d”) and the torque decreases to zero. From “d” to “g” (leaving the corner and approaching the axis of the tube), although the torque acting on the particle is negative, it rotates counterclockwise continuously due to the inertia. At the state “h,” the negative torque becomes weak and the particle is very close to the horizontal orientation ($\gamma = 84.7^\circ$ at point “h”). Due to inertia effect again, the particle continuously rotates counterclockwise and across the horizontal orientation at time $t \approx 4320$. This is the end of this period and then another period will begin. Hence, the inertia of the ellipsoid plays an important role in inducing the anomalous mode.

The effects of geometry and density on the angle γ_a when it moves across the axis of the tube are shown in Table II. For the square tubes, before the oscillatory mode translates to the anomalous mode, the maximum $(\gamma_a)_m$ are approximately 88° (almost horizontal) for tubes with $\frac{D}{A} = \frac{20}{13}$ and $\frac{26}{13}$. It is a favorable orientation which may induce the anomalous mode. For a slightly higher rotational inertia (slightly larger ρ_p), the ellipsoid may rotate through the horizontal orientation and the anomalous mode appears. On the contrary, for narrow tubes $\frac{D}{A} \leq \frac{16}{13}$, $(\gamma_a)_m$ is not close to 90° enough of the time and the anomalous mode does not occur.

From Table II, we can also see the effect of inertia. For example, in the square tube with $\frac{D}{A} = \frac{20}{13}$, and a lower inertia ($\frac{\Delta\rho}{\rho_f} = 0.02$), we have an oscillatory mode. However, a slightly higher inertia

TABLE II. The effect of geometry and density of particle on γ_a , which is the angle between the x' - and z -axis when it moves across the axis of the tube (Osc., Inc., and Ano. denote the oscillatory, inclined, and anomalous modes, respectively).

Tube type	D/A	$\frac{\Delta\rho}{\rho_f}$	Mode	γ_a	D/A	$\frac{\Delta\rho}{\rho_f}$	Mode	γ_a	D/A	$\frac{\Delta\rho}{\rho_f}$	Mode	γ_a
Square	$\frac{16}{13}$	0.08	Osc.	76.3°	$\frac{20}{13}$	0.01	Osc.	83.6°	$\frac{26}{13}$
	$\frac{16}{13}$	0.15	Osc.	79.7°	$\frac{20}{13}$	0.015	Osc.	84.6°	$\frac{26}{13}$	0.001	Osc.	85.3°
	$\frac{16}{13}$	0.18	Osc.	80.7°	$\frac{20}{13}$	0.02	Osc.	87.6°	$\frac{26}{13}$	0.002	Osc.	87.5°
	$\frac{16}{13}$	0.22	Inc.	...	$\frac{20}{13}$	0.025	Ano.	...	$\frac{26}{13}$	0.003	Ano.	...

($\frac{\Delta\rho}{\rho_f} = 0.025$) makes the particle rotate across the horizontal orientation when it approaches the z -axis and the motion mode shifts to the anomalous mode.

For circular tubes, we carried out systematic simulations but the anomalous mode is not found. One possible reason is that the combination of the inertial and geometric effects is not so perfect as that in square tubes to allow this mode to appear.

VII. CONCLUSION

The sedimentation of an ellipsoid inside both circular and square tubes has been studied numerically. The phase diagram of the flow regimes as functions of the tube diameter and Re (or density ratio) are obtained. For the circular tubes $D < A$, the spiral and vertically inclined modes are observed. Near transitional regimes (oscillatory mode changing to inclined mode), for a circular tube $\frac{D}{A} = \frac{16}{13}$, the average sedimentation velocity of a lighter particle may be larger than that of a heavier one. The possible reason is revealed. For square tubes, the ellipsoid may adopt the anomalous mode, which usually occurs inside tubes with $D > 1.4A$ and $Re \sim O(1)$. Two critical factors that result in this mode are identified: one is the geometry of the tube, the other is the inertia of the particle.

Based on limited observation, it seems that all modes are independent of the initial orientation or location. It is an open question whether there exist modes of settling that depend on the initial configuration. We will carry out the study in the near future.

ACKNOWLEDGMENTS

H. Huang is supported by National Natural Science Foundation of China (Grant No. 11172297), Anhui Provincial Natural Science Foundation (Grant No. 1308085MA06), and Program for New Century Excellent Talents in University, Ministry of Education, China (NCET-12-0506).

- ¹G. B. Jeffery, "The motion of ellipsoidal particles immersed in a viscous fluid," *Proc. R. Soc. London, Ser. A* **102**, 161 (1922).
- ²A. Karnis, H. L. Goldsmith, and S. G. Mason, "The flow of suspensions through tubes. Part 5: Inertial effects," *Can. J. Chem. Eng.* **44**, 181 (1966).
- ³D. Broday, M. Fichman, M. Shapiro, and C. Gutfinger, "Motion of spheroidal particles in vertical shear flows," *Phys. Fluids* **10**, 86 (1998).
- ⁴H. Liu, H. H. Bau, and H. H. Hu, "On the translation of a cylinder in a long tube," *Phys. Fluids* **16**, 998 (2004).
- ⁵R. G. Cox, "The steady motion of a particle of arbitrary shape at small Reynolds numbers," *J. Fluid Mech.* **23**, 625 (1965).
- ⁶W. B. Russel, E. J. Hinch, L. G. Leal, and G. Tieffenbruck, "Rods falling near a vertical wall," *J. Fluid Mech.* **83**, 273 (1977).
- ⁷J. F. Brady and G. Bossis, "Stokesian dynamics," *Ann Rev. Fluid Mech.* **20**, 111 (1988).
- ⁸M. Sugihara-Seki, "The motion of an ellipsoid in tube flow at low Reynolds numbers," *J. Fluid Mech.* **324**, 287 (1996).
- ⁹T. N. Swaminathan, K. Mukundakrishnan, and H. H. Hu, "Sedimentation of an ellipsoid inside an infinitely long tube at low and intermediate Reynolds numbers," *J. Fluid Mech.* **551**, 357 (2006).
- ¹⁰R. Glowinski, T. W. Pan, T. I. Hesla, D. D. Joseph, and J. Périaux, "A fictitious domain approach to the direct numerical simulation of incompressible viscous flow past moving rigid bodies: Application to particulate flow," *J. Comput. Phys.* **169**, 363 (2001).
- ¹¹E. Ding and C. K. Aidun, "The dynamics and scaling law for particles suspended in shear flow with inertia," *J. Fluid Mech.* **423**, 317 (2000).
- ¹²Z. Xia, K. W. Connington, S. Rapaka, P. Yue, J. J. Feng, and S. Chen, "Flow patterns in the sedimentation of an elliptical particle," *J. Fluid Mech.* **625**, 249 (2009).
- ¹³H. Huang, X. Yang, M. Krafczyk, and X.-Y. Lu, "Rotation of spheroidal particles in Couette flows," *J. Fluid Mech.* **692**, 369 (2012).
- ¹⁴C. M. Zettner and M. Yoda, "Moderate-aspect-ratio elliptical cylinders in simple shear with inertia," *J. Fluid Mech.* **442**, 241 (2001).
- ¹⁵D. Qi and L.-S. Luo, "Rotational and orientational behaviour of a three-dimensional spheroidal particles in Couette flows," *J. Fluid Mech.* **477**, 201 (2003).
- ¹⁶J. Feng, H. H. Hu, and D. D. Joseph, "Direct simulation of initial-value problems for the motion of solid bodies in a Newtonian fluid. I. Sedimentation," *J. Fluid Mech.* **261**, 95 (1994).
- ¹⁷D. Karamanev, C. Chavarie, and R. Mayer, "Dynamics of the free rise of a light solid sphere in liquid," *AIChE J.* **42**, 1789 (1996).
- ¹⁸P. Ern, F. Risso, D. Fabre, and J. Magnaudet, "Wake-induced oscillatory paths of bodies freely rising or falling in fluids," *Ann. Rev. Fluid Mech.* **44**, 97 (2012).
- ¹⁹F. Auguste, J. Magnaudet, and D. Fabre, "Falling styles of disks," *J. Fluid Mech.* **719**, 388 (2013).

- ²⁰T. Deloze, Y. Hoarau, and J. Dušek, "Transition scenario of a sphere freely falling in a vertical tube," *J. Fluid Mech.* **711**, 40 (2012).
- ²¹A. J. C. Ladd, "Numerical simulations of particulate suspensions via a discretized Boltzmann equation. Part 1. Theoretical foundation," *J. Fluid Mech.* **271**, 285 (1994).
- ²²A. J. C. Ladd, "Numerical simulations of particulate suspensions via a discretized Boltzmann equation. Part 2. Numerical results," *J. Fluid Mech.* **271**, 311 (1994).
- ²³C. K. Aidun, Y. Lu, and E. E. Ding, "Direct analysis of particulate suspensions with inertia using the discrete Boltzmann equation," *J. Fluid Mech.* **373**, 287 (1998).
- ²⁴P. Lallemand and L.-S. Luo, "Lattice Boltzmann method for moving boundaries," *J. Comput. Phys.* **184**, 406 (2003).
- ²⁵D. d'Humières, I. Ginzburg, M. Krafczyk, P. Lallemand, and L.-S. Luo, "Multiple-relaxation-time lattice Boltzmann models in three dimensions," *Philos. Trans. R. Soc. Lond A* **360**, 437 (2002).
- ²⁶M. Bouzidi, M. Firdaouss, and P. Lallemand, "Momentum transfer of a Boltzmann-lattice fluid with boundaries," *Phys. Fluids* **13**, 3452 (2001).
- ²⁷R. Mei, D. Yu, W. Shyy, and L.-S. Luo, "Force evaluation in the lattice Boltzmann method involving curved geometry," *Phys. Rev. E* **65**, 041203 (2002).
- ²⁸Z.-G. Feng and E. E. Michaelides, "The immersed boundary-lattice Boltzmann method for solving fluid-particles interaction problems," *J. Comput. Phys.* **195**, 602 (2004).
- ²⁹A. J. C. Ladd and R. Verberg, "Lattice-Boltzmann simulations of particle-fluid suspensions," *J. Stat. Phys.* **104**, 1191 (2001).
- ³⁰O. Filippova and D. Hänel, "Grid refinement for lattice-BGK models," *J. Comput. Phys.* **147**, 219 (1998).
- ³¹C. K. Aidun and E. Ding, "Dynamics of particle sedimentation in a vertical channel: Period-doubling bifurcation and chaotic state," *Phys. Fluids* **15**, 1612 (2003).
- ³²A. Karnis, H. L. Goldsmith, and S. G. Mason, "Axial migration of particles in Poiseuille flow," *Nature (London)* **200**, 159 (1963).
- ³³Y. J. Liu, J. Nelson, J. Feng, and D. D. Joseph, "Anomalous rolling of spheres down an inclined plane," *J. Non-Newtonian Fluid Mech.* **50**, 305 (1993).